Research Article Vol. 32, No. 27 / 30 Dec 2024 / *Optics Express* 48525

Optics EXPRESS

Alignment of a Ritchey-Chrétien telescope with primary mirror figure error guided by the rapid measurement of binodal astigmatism

NIKOLAS ROMER,[1,*] NAN ZHAO,[1,2] ÖZGÜR KARCI,[3] AND JANNICK P. ROLLAND[1]

[1] *Institute of Optics, University of Rochester, Rochester, NY 14620, USA*
[2] *Changchun Institute of Optics and Fine Mechanics and Physics, Chinese Academy of Sciences, Changchun, Jilin 130033, China*
[3] *TÜBİTAK Space Technologies Research Institute, METU Campus, 06800, Çankaya, Ankara, Turkey*
[*] *nromer@ur.rochester.edu*

Abstract: Nodal aberration theory (NAT) is a vectorized aberration theory that was developed to describe systems without rotational symmetry. NAT predicts non-rotationally symmetric aberration field dependences for third-order astigmatism and in particular a "binodal" behavior in which there are two points in the field of view where astigmatism vanishes. This study serves to demonstrate an alignment technique based on an understanding of this binodal behavior using a custom Ritchey-Chretien telescope. A method involving a commercial Shack-Hartmann compact-format wavefront sensor was developed to rapidly measure densely sampled full-field displays of the telescope, which has its secondary mirror mounted on a precision hexapod to allow for repeatable control of the telescope alignment. Real ray-based simulations were carried out on a model of the telescope and were consistent with the observed experimental results for both aligned and misaligned states of the telescope. We then provide guidelines on how to interpret Fringe Zernike astigmatism full-field displays for use during optical system alignment. This method is particularly relevant for freeform systems, which often have asymmetric field dependencies for multiple aberration types including astigmatism.

1. Introduction

Nodal aberration theory was invented by R.V. Shack and developed by K.P. Thompson to describe the field dependence of third order aberrations in optical systems without symmetry [1]. Thompson laid out the vectorized descriptions for the third order aberrations in [2], where he also shows that no new types of aberrations appear as a result of misalignment. While the original application was to describe misaligned systems, the theory has since been extended to describe freeform optical surfaces and is the basis for cutting edge freeform optical design methods today [3–6]. The history of the progression from NAT's initial development to its application to freeform is covered in [7].

In [2] Thompson describes the generalized third order astigmatism as

$$W_{astig} = \frac{1}{2}\sum_{j} W_{222j}[(\boldsymbol{H}-\sigma_{\mathbf{j}})\cdot\boldsymbol{\rho}^{2}] = \frac{1}{2}\left[\sum_{j} W_{222j}\boldsymbol{H}^{2} - 2\boldsymbol{H}\left(\sum_{\boldsymbol{j}} W_{222j}\boldsymbol{\sigma_{j}}\right) + \sum_{\boldsymbol{j}} W_{222j}\boldsymbol{\sigma}_{\boldsymbol{j}}^{2}\right]\cdot\boldsymbol{\rho}^{2}. \quad (1)$$

where W_{222j} is the third order contribution to astigmatism from the jth surface, $\boldsymbol{\rho}$ is the normalized pupil coordinate vector, and $\boldsymbol{H}$ is the normalized field coordinate vector. Vector quantities are indicated in bold. The misalignment vector $\boldsymbol{\sigma_j}$ is used to describe the shift of the aberration field contribution from each surface. The first term in the expanded form of Eq. (1) is the third order astigmatism in the absence of misalignments. From the following two terms, misalignment

#541050 https://doi.org/10.1364/OE.541050
Journal © 2024 Received 3 Sep 2024; revised 1 Nov 2024; accepted 5 Nov 2024; published 20 Dec 2024

vectors $\boldsymbol{A}_{222}$ and $\boldsymbol{B}^2_{222}$ are defined as

$$\mathbf{A}_{222} = \sum_j \boldsymbol{\sigma_j} W_{222j} \tag{2a}$$

$$\boldsymbol{B}^2_{222} = \sum_j \sigma^2_{\mathbf{j}} W_{222j}. \tag{2b}$$

The normalized versions of the vectors $\boldsymbol{a}_{222}$ and $\boldsymbol{b}^2_{222}$ can be calculated by dividing the unnormalized versions by W_{222}. Noting that the expanded form in Eq. (1) is quadratic with $\boldsymbol{H}$, the normalized misalignment vectors can be used to locate the zeros or "nodes" of astigmatism in the field of view. The first vector $\boldsymbol{a}_{222}$ points from the origin to the midpoint between the two astigmatic nodes, while $\boldsymbol{b}_{222}$ points from that midpoint to each of the node locations, as illustrated in Fig. 1.

In addition to misalignment, the introduction of astigmatic figure error onto mirror surfaces can also affect the field dependence of astigmatism, and notably the location of the nodes. Thus, we now redefine the vector $\boldsymbol{B}^2_{222}$ in two parts to separate the contributions from misalignment and figure error. Note that the squared vectors indicate Shack vector products, which are defined in an appendix of [2].

$$\boldsymbol{B}^2_{222} = \boldsymbol{B}^2_{222-ALIGN} + \boldsymbol{B}^2_{222-\boldsymbol{FIGERR}} \tag{3}$$

The node shifts due to pure astigmatic figure error without misalignment can be calculated using the following formulas, which were derived in [8].

$$\boldsymbol{B}^2_{222-\boldsymbol{FIGERR}} = 2Z_{(5/6)} exp(2i\xi_{(5/6)}) \tag{4}$$

$$\xi_{(5/6)} = \frac{1}{2} \arctan\left(-\frac{Z_6}{Z_5}\right) \tag{5}$$

$$Z_{5/6} = \sqrt{Z_5^2 + Z_6^2} \tag{6}$$

where Z_5 and Z_6 are the coefficients of the fifth and sixth Zernike polynomials that represent third order astigmatism in the Fringe ordering convention and $Z_{5/6}$ is the combined magnitude. In this context, the Zernike polynomials are used to describe the error of the surface from its nominal shape, where $\xi_{(5/6)}$ represents the clockwise azimuthal rotation of the $\pm\boldsymbol{b}_{222}$ vectors from the horizontal, where $\boldsymbol{b}_{222}$ is the normalized $\boldsymbol{B}_{222}$ by the W_{222} system astigmatism. For a telescope with its stop located at the primary mirror with astigmatic figure error, each field will have the same mirror footprint and thus acquire the same aberration from the figure error. Thus, field-constant (FC) astigmatism is the result when there is astigmatic figure error on the telescope primary mirror.

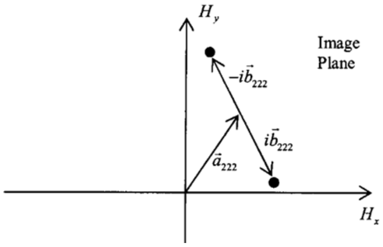

Fig. 1. Location of astigmatic nodes as described by Nodal Aberration Theory. Adapted with permission from [2] © Optical Society of America.

FC astigmatism, depending on its magnitude, may cause binodal behavior when combined with other field dependence astigmatism even without misalignments. A nominally aligned Ritchey-Chretien telescope (RC) will have a field-quadratic, rotationally symmetric pattern. With the introduction of FC astigmatism, there will be two points where both the magnitude and the direction of the astigmatism are such that cancellation occurs, leading to the binodal behavior. This cancellation is described in detail by Schmid in [9]. Without misalignments ($\boldsymbol{\sigma_j} = 0$), we see that $\boldsymbol{A}_{222}$ will be zero, so any nodes due to figure error will always be symmetric about the on-axis field.

In [10], an RC telescope was constructed and used to demonstrate the field dependence of third order coma in the presence of misalignments. Karci *et al.* then demonstrated the binodal behavior of astigmatism on a Cassegrain telescope [11], and the separation of those measurements from figure error contributions in [12]. In this work, we follow Zhao and Karci to demonstrate how the field dependence of astigmatism can be utilized in the alignment of an RC telescope. We demonstrate this technique in the presence of primary mirror figure error, although its utility is not limited to RC telescopes or systems with figure error.

While the field dependence of aberrations in misaligned systems has been understood for some time, the practicality of measuring aberrations through a large number of field points – particularly with interferometry – has long been a limitation. In this paper, we first detail in Section 2 how to qualitatively interpret Zernike astigmatism FFDs for use during alignment. Section 3 reviews the design and assembly of the Hilbert telescope. In Section 4, we report on a new experimental setup that includes the automation of data acquisition and stage movement of a compact wavefront sensor to enable rapid measurements across a 0.40-deg. full field of view with a spacing of 0.036 deg. To allow rapid movement between field points, a lightweight, integrated Shack-Hartmann wavefront sensor was leveraged. The methodology demonstrated allows for the lessons from NAT to be used more practically in alignment, employing the qualitative methods from Section 2. Section 5 concludes on our lessons from the study.

2. Using astigmatism full field displays for alignment

2.1. Interpreting binodal astigmatic fields for a Ritchey-Chretien telescope

Nodal aberration theory enables us to predict the location of astigmatic nodes in a telescope's field of view using first and third order quantities. In the context of aligning an RC telescope, if the astigmatic figure error on the primary mirror is known and we are able to locate the two astigmatic nodes, we can calculate the secondary mirror misalignment [9]. Others have used these principles in alignment by measuring a few points in the field of view to estimate node locations. The original alignment plan for the Large Synoptic Survey Telescope (LSST) employed precision laser tracking systems to monitor the positions of mirrors and reduce errors in the node calculation process [13]. In this work, we measure a large number of field points in order to see direct evidence of the astigmatic nodes – removing the need for external monitoring of the mirror positions in space. However, nodes can be located asymmetrically about the on-axis field and even beyond the measurable or designed field of view, depending on the severity of misalignment. To restore the telescope to a state of alignment where the nodes can be located with high precision, we must understand how to qualitatively interpret measured field dependencies of astigmatism where nodes may not be obvious.

We examine the case of a two-mirror RC telescope first where the mirrors are assumed to be polished nominally and thus have negligible figure error. The aperture-stop and the global coordinate systems are both centered on the primary mirror, meaning that any misalignment terms from the primary mirror are always zero. A nominally aligned RC telescope has a rotationally symmetric astigmatism field for which the magnitude increases quadratically with the normalized field coordinate H. We can equivalently describe this as the two astigmatic nodes being coincident and located at the on-axis point.

When the secondary mirror is misaligned, the astigmatism field becomes binodal. Provided the misalignment is small, one node will be located at or very close to $\boldsymbol{H} = (0, 0)$ while the other will be displaced by a misalignment vector described by $\boldsymbol{a}_{222} \pm i\boldsymbol{b}_{222}$. For larger misalignments, neither node will be located at the origin unless the secondary mirror has been aligned to remove field-constant coma [8]. In this work, we use full field displays (FFDs) to represent the magnitude and orientation of astigmatism over a field of view of interest. All FFDs shown are generated using a Fringe Zernike polynomial fit over the pupil for a given field point. Note that some other works present FFDs using the astigmatic line image rather than the aberrations in the pupil, which leads to a 90-deg. rotation of the icons in the display [2]. The 5th and 6th coefficients are used to estimate the magnitude ($Z_{5/6}$) and orientation of astigmatism (θ_{ASTIG}), which are indicated by the length and orientation of the icons. θ_{ASTIG} is the clockwise angle with respect to the positive Y-axis given as

$$\theta_{ASTIG} = 90 - \frac{1}{2}\tan^{-1}\left(\frac{Z_6}{Z_5}\right) \tag{7}$$

Figure 2 shows examples of third-order astigmatism FFDs for an RC telescope in each of the cases mentioned above generated with the Z_5 and Z_6 Fringe Zernike coefficients in the pupil.

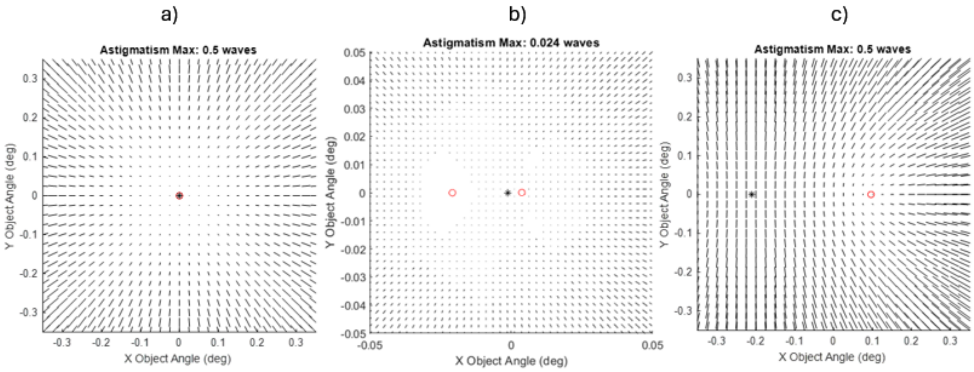

Fig. 2. a) Nominal Astigmatism FFD for an aligned Ritchey-Chretien telescope. b) Astigmatic node shift for a small misalignment of 0.02 deg., shown over a smaller FOV and different scale for visibility. c) Larger node shift for a 0.5 deg. secondary mirror tilt misalignment. Open red circles denote node locations, and the asterisk (black) represents the point of symmetry between the nodes. Simulated using real ray traces in CODEV.

To allow us to later make sense of measured pupil FFDs, we draw an analogy from electromagnetism where each node represents a like magnetic pole (e.g., North-North), and the astigmatism icons are analogous to the resulting magnetic vector field. Once we visualize the associated "field lines," we can rely on the following characteristics of binodal astigmatism fields:

1. There are always two nodes (unless they are coincident at the origin).
2. At the point of symmetry (POS), the field line will be straight and perpendicular to $\pm\boldsymbol{b}_{222}$
3. If tracing over $\boldsymbol{b}_{222}$, the local astigmatism orientation will rotate by 90 deg. after crossing over the node as shown in Fig. 3.
4. Astigmatism magnitudes surrounding a node will approach a local minimum.

For a real-world alignment scenario, the third case in Fig. 2 with large misalignments is often relevant. In such a scenario, the extent of the measurable field of view may be limited, and the density of measured field points will also be limited depending on the measurement technique.

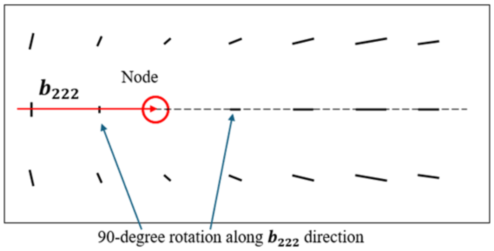

Fig. 3. Close up of the area surrounding an astigmatic node simulated with real rays in CODE V. The 90-deg. rotation implies the presence of an astigmatic node.

A consequence of these limitations will be that the nodes or other features may not be obvious or located within the measured portion of the field of view. However, we can use the above framework to infer the node and POS locations even if they are not directly measured.

In Fig. 4 we re-examine the most severely misaligned case from Fig. 2, with guiding field lines drawn. In the smaller field of view shown in Fig. 4(b), which mimics the accessible field of view in our measurements below, we see that the point of symmetry and perpendicular field line are now out of view. By examination of the one visible node and the "straightening" of the field lines as we move left from the node, we can infer that both the POS and second node exists outside of the field of view in the negative X-object angle direction. This implies that a tilt or decenter action along this same axis can be used to move the POS back to the center of the field of view.

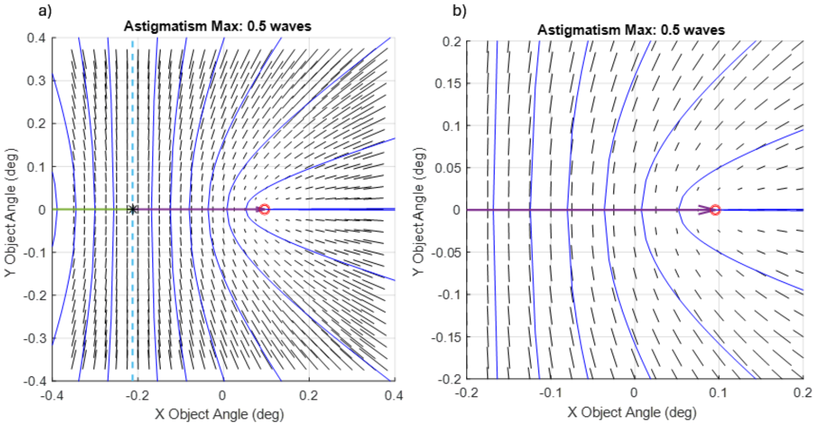

Fig. 4. a) 0.5 deg.-misaligned case from Fig. 2 drawn with approximate field lines. b) Central 0.4° section of the FFD on the left, which is the maximum available field of view on our testbed. "Field lines" are drawn in blue, $\pm b_{222}$ arrows point in green and purple from the POS, and the perpendicular field line passing through the point of symmetry is the dashed light blue line. Open red circles denote nodes and the asterisk represents the POS

By understanding this structure of general binodal astigmatism fields, one can infer the locations of astigmatic nodes even without directly measuring both node locations. It is not necessary to always draw field-lines, but it can be a useful practice to deepen insight. It is necessary, however, to sample the field densely enough to reveal the magnetic field-like structure for this method to be useful in alignment. In Section 4.4, we use this framework to align an RC telescope.

2.2. Sampling considerations within the full field of view

When interpreting FFDs in the method discussed in Section 2.1, the POS and nodes are often identified inferentially as they can lie between two measured points. Thus, the error in the inferred node or POS location is determined by the spacing between measured points. If the full field of view is not sampled sufficiently, an FFD may appear aligned even in the presence of small residual misalignments. We can see such a case in Fig. 5(a) and 5(b), where both the aligned and 0.05° tilt case appear virtually identical. Normally distributed random noise with a standard deviation of 0.02λ has been added to the Zernike coefficients in the simulation based on the stability measurements reported in Section 4.3.

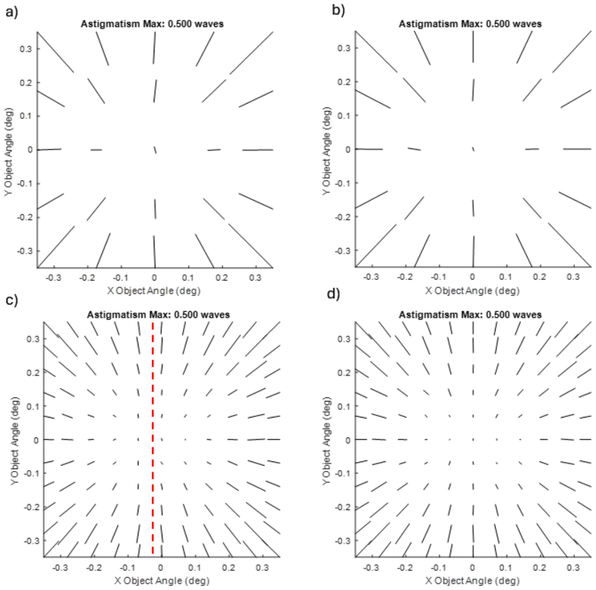

Fig. 5. Simulated astigmatism FFDs with added measurement noise (i.e., normal distribution with 0.02λ standard deviation) for a) 0.05-degree secondary mirror tilt and 5×5 grid, b) no misalignment and 5×5 grid, c) 0.05-degree secondary mirror tilt and 11×11 grid, d) no misalignment and 11×11 grid. The dashed line in c) indicates the inferred X coordinate of the point of symmetry.

In Fig. 5(c), we can see the finer sampling reveals that the POS is between the central column and the column at -0.07° in X, where the red dash line is drawn. Inspection of the FFD structure reveals not only the presence of misalignment, but the location of the POS down to ±0.035°.

2.3. Effects of primary mirror figure error

As discussed above, astigmatic figure error on the primary mirror/stop surface of an RC telescope will create a binodal structure in the astigmatism FFD even in the absence of any misalignments. For an aligned RC telescope with astigmatism on its stop surface, we expect to have two nodes symmetric about the origin. The orientation of these two nodes depends on the clocking of the astigmatic figure error, and the distance from the origin depends on the magnitude. Since $\boldsymbol{a}_{222}$ is not dependent on primary mirror figure error, any asymmetry (nonzero $|\boldsymbol{a}_{222}|$) about the origin implies there is also misalignment present. Freeform optical systems often have binodal or non-axisymmetric astigmatism FFDs in their nominal configurations, thus making the following a useful exercise to consider alignment scenarios where the end goals are to achieve a specific structure in an aberration FFD rather than just minimizing aberrations [5]. Figure 6 is an example of an FFD for a telescope that is aligned but contains astigmatic figure error on its stop surface.

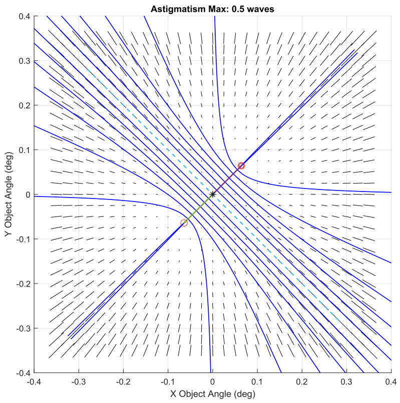

Fig. 6. An example of a binodal astigmatism FFD for form error, which is symmetric about the origin. "Field lines" are drawn in blue, $\pm\boldsymbol{b}_{222}$ arrows point in green and purple from the origin, and the perpendicular field line passing through the point of symmetry is the dashed light blue line. Open red circles denote nodes and the asterisk represents the POS.

3. Hilbert memorial telescope

The telescope used in this work is a two-mirror RC type telescope that consists of hyperbolic primary and secondary mirrors. The prescription of the telescope and a ray drawing are given in Table 1 and Fig. 7, respectively. The entrance pupil diameter is 304.8 mm, and its f-number is 8.6. The primary mirror is the aperture stop surface.

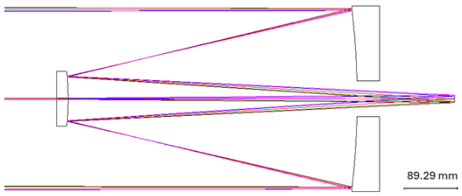

Fig. 7. CODE V ray trace of Hilbert memorial telescope.

Table 1. Prescription of Hilbert Memorial Telescope

Surface	RoC (mm)	Thickness (mm)	Conic constant, k
M1	-1291.2	-485.5	-1.06
M2	-425.0	649.3	-3.31

The secondary mirror (M2) of the telescope is mounted on a hexapod (Physik Instrumente H-810) positioner robot that has a tilt repeatability of ±3 μrad, and XY translational repeatability of 1 μm [14]. The truss structure that holds M2 will have some deflection caused by gravity, so the hexapod can be used to compensate for this deflection as well as for general alignment.

A nominally built and aligned RC telescope uses conic surfaces to correct third order spherical aberration and third order coma over the field of view. It is also common to introduce refractive field-flattening lenses near the focal plane, but these are not considered in this experiment. Due to our measurement configuration, the secondary mirror of the telescope contains despace error that contributes field-constant spherical aberration and field-linear coma into the system. However, this error does not affect the location of astigmatic nodes in the aberration fields, which is the focus of this study.

When the Hilbert telescope was built, the primary mirror was measured using an Offner null test configuration [10]. The mirror exhibits some astigmatic figure error as shown in Fig. 8, which was left from the polishing process. The null test was measured using a DynaFiz Fizeau interferometer from Zygo Corporation.

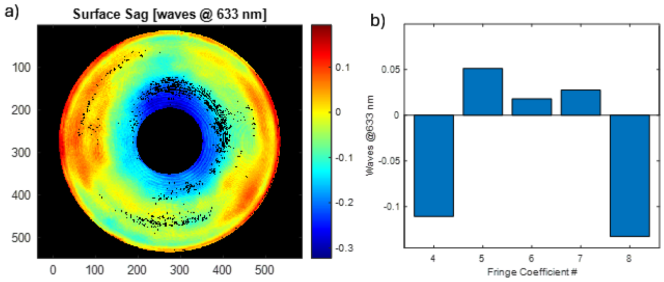

Fig. 8. a) Sag from Offner null test of Hilbert telescope primary mirror. Piston, tip, tilt, and coma from misalignment have been removed [10]. b) Fringe Zernike coefficients fit to the sag measurement before subtraction of PTT and coma terms.

A Fringe Zernike polynomial fit was carried out with the resulting coefficients shown on Fig. 8. The coma terms are a result of misalignments in the null test measurement and have been removed from the surface sag shown above [15]. Because the primary mirror is the aperture stop of the telescope, these aberrations are transmitted in a field-constant manner and will appear as such in the aberration FFDs. As mentioned above, we expect to see a cancellation that occurs at two points (nodes) in the astigmatism FFD whose location will depend on the relative orientation of the figure error and its magnitude. The measured figure error from the Offner null test was placed onto the primary mirror in CODE V and the simulated aberration FFDs were computed in Fig. 9, exhibiting the expected binodal behavior. Additionally, we see agreement with the predicted node locations from Eqs. (4) and (5).

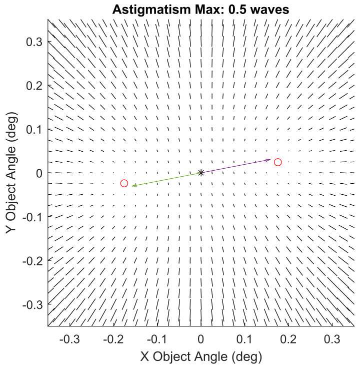

Fig. 9. Zernike astigmatism FFD simulated for the Hilbert RC telescope the primary form error measured and shown in Fig. 8. Arrows indicate the node locations predicted by Eqs. (4) and (5) based on the measured astigmatism form error, and circles indicate the minima found numerically in CODE V. The asterisk is the point of symmetry between the two nodes.

4. Hilbert telescope alignment campaign

4.1. Testbed

The field dependent aberrations of the telescope were measured in a double pass configuration, shown in Fig. 10. A HASO LIFT680 Shack-Hartmann wavefront sensor was integrated with a red (635 nm) laser source and the F60 objective lens (EFL = 60 mm, F/6) and mounted such that the focus was coincident with the telescope focus. This assembly (RFLEX) is an off-the-shelf product provided by Imagine Optic, and has a repeatability of $\lambda/200$. [16]. The RFLEX is placed such that the Shack-Hartmann lenslet array is conjugate to the telescope pupil, meaning that all wavefront measurements are taken in the pupil.

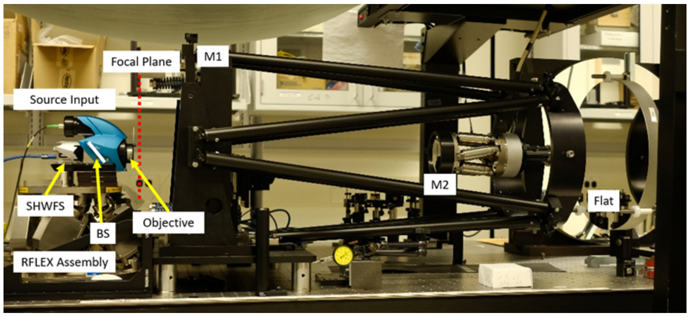

Fig. 10. Metrology Setup for FFD Measurements of the Hilbert Memorial Telescope.

The RFLEX assembly is mounted on a second hexapod positioner (PI H-824) which allows for precise and automated scanning through different field positions in the telescope back focal plane [17]. The H-824 has a vertical repeatability of ±0.1 μm, a horizontal repeatability of ±0.25 μm, and a tilt repeatability of ±2.0 μrad. The hexapod is positioned such that the focus of the objective lens is coincident with the focus of the on-axis field of the telescope when the actuators are at the center of their travel to maximize range.

A real ray trace was performed on the nominal (misalignment and figure error-free) model of the telescope in CODE V to determine the X-Y position and the chief ray angles for an 11×11 grid of points in the telescope's field of view. After the chief ray angles are rotated into the hexapod coordinate frame, the hexapod is provided a list of position vectors (X, Y, X-rotation, Y-rotation) that correspond to the grid of field points. The fields are scanned in a semi-automated manner and with each field the reference flat mirror must be adjusted to minimize tip and tilt before recording the wavefront slopes. Each measurement required around 45 seconds to complete, leading to roughly a 45-minute measurement time for a 0.4-deg. full field of view set spaced at every 0.036 deg. Some field points around the periphery of the 11×11 grid are omitted because they were out of range of the H-824 Hexapod.

4.2. Wavefront fitting and error estimation

For each measured field position, a set of wavefront slopes was recorded by the Shack-Hartmann sensor and reconstructed using a Zernike-based modal reconstruction method built into the instrument software provided by Imagine Optic [16]. Wavefront data was then fit to Fringe Zernike polynomials using the ZernikeCalc function in MATLAB [12]. Examples of raw and processed wavefronts are presented in Fig. 11.

The Hilbert telescope's pupil is obscured not only by the secondary mirror, but also by support spiders and cabling that are necessary for operation of the hexapod on the secondary mirror. The support spiders were thin enough that it was deemed appropriate to interpolate over this missing data within the Imagine Optic software environment. Software masks were applied

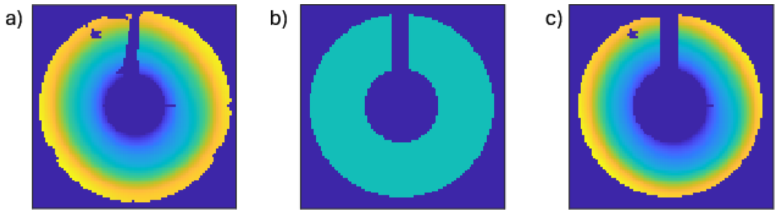

Fig. 11. a) Raw wavefront exported from Imagine Optic "Waveview" software. The obscuration from hexapod cabling is visible at the top. b) Mask applied to all wavefronts to reduce fit variability due to cable and central obscurations. c) Masked wavefront data.

to reduce variability between measurements that could arise from the cabling obscuration or mounting-related obscurations at the edges. All wavefronts are then fit to the Fringe Zernike coefficient set, and the FFD is generated to represent the magnitude and orientation of astigmatism at each given field point.

Both the cabling and central obscurations cause degeneracy when fitting to the Fringe Zernike polynomial set, which is orthogonal over a circular pupil. The central obscuration mainly causes degeneracy across the rotationally symmetric Zernike terms, i.e. piston, defocus, third-order spherical, and higher orders of spherical aberration. Due to its placement, the cabling obscuration can cause more degeneracy in non-rotationally symmetric Zernike terms such as astigmatism and coma.

A Monte-Carlo analysis was performed to assess the errors caused by fitting the irregular pupil shape over a circular pupil. A set of the first 25 randomized Zernike polynomial coefficients between -1 and +1 waves was used to generate a wavefront over a circular pupil. A mask identical to the one used in experiment was then applied to the wavefront, and then the resulting obscured wavefront was fit over the original circular pupil. Figure 12 shows a bar graph of the maximum error between the input coefficient and the coefficient from fitting after the mask was applied over 600 trials.

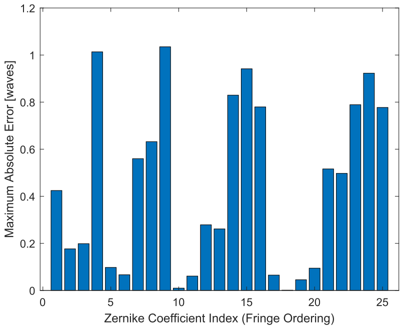

Fig. 12. Maximum observed absolute error between input Zernike coefficient values and values from fitting after application of the non-circular mask. Results shown from 600 iterations of randomized input coefficients between -1 and +1 waves.

Over 600 iterations of randomized input Zernike coefficients, we observe the largest maximum errors in the rotationally symmetric terms piston (Z_1), defocus (Z_4), third-order spherical (Z_9), and fifth-order spherical (Z_{16}). There is also some tilt (Z_2, Z_3), coma (Z_7, Z_8), and fifth-order coma (Z_{14}, Z_{15}) degeneracy observed, likely because of the asymmetric placement of the cable obscuration. For astigmatism (Z_5, Z_6), which is of most interest in this study, we see maximum absolute errors over 600 iterations of 0.16λ for Z_5 and 0.07λ for Z_6. The mean absolute errors for Z_5 and Z_6 were 0.04λ and 0.02λ, and the respective standard deviations were 0.05λ and 0.03λ.

4.3. Testbed environment and stability

Characterization of the testbed environment was performed to assess the stability of the telescope over the time duration of each FFD measurement set, which was about 45 minutes. Short-term fluctuations due to in-lab turbulence, and long-term drifts due to ambient temperature changes and actuator creep were considered. Aberrations were measured over a five-minute period every ten seconds for short-term fluctuations (Fig. 13(a)) and a two-hour period every minute for long-term fluctuations (Fig. 13(b)).

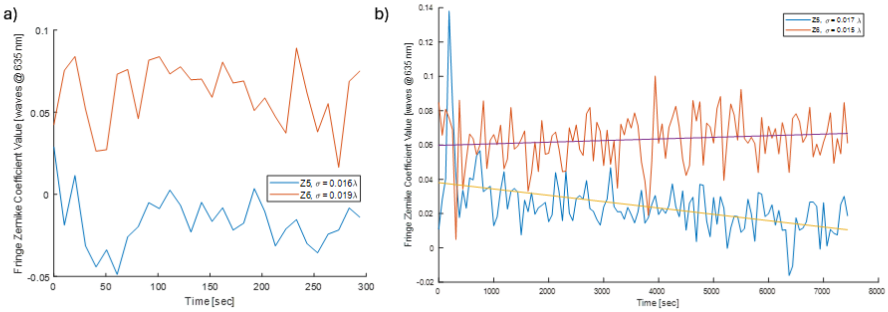

Fig. 13. a) Short-term aberration stability measurements to assess the effects of air turbulence. Recorded over a period of 5 minutes. Standard deviations (σ) are given in the legend. b) Long-term stability measurements to assess the effects of drifts due to ambient temperature fluctuations and the piezoelectric actuators in both hexapod positioners. Recorded over a period of two hours. Linear trendlines are plotted to show the long-term drifts observed.

The results in the following section were collected over intervals of around 45 minutes for each FFD. Both the fifth and sixth Fringe Zernike terms have standard deviations (σ) less than $\lambda/50$ for $\lambda = 635$ *nm* in both the short-term and long-term stability trials. Assuming that these random fluctuations follow a normal distribution, 95% of measurements should be within 2σ of the mean or $\lambda/25$. These fluctuations are responsible for the slight variations seen in the local orientations and magnitude of the measured FFD icons shown below. However, they are not large enough to obscure our ability to recognize the features of the FFDs necessary for interpretation. The long-term stability trial found slight drifts of both coefficients over the two-hour monitoring period. Linear regression found slopes of -0.013 waves/hour and 0.0034 waves/hour (@ 635 nm) for the Z_5 and Z_6 coefficients, respectively. Such drifts are also not large enough to obscure the features of interest during alignment. Greater stability may be necessary for any future applications where more accurate determination of a node's location is required.

4.4. Telescope alignment

A commonly used optical alignment strategy is to position optics such that both coma and astigmatism through the system are minimized at the on-axis field. As a consequence of the known figure error on the primary mirror of the telescope, the Hilbert telescope's on-axis field does not have zero astigmatism. Thus, a modified alignment strategy was adopted that employed the insights provided by astigmatism FFD measurements.

To first roughly align the telescope, the RFLEX's output was visually aligned to the primary mirror using the H-824 Hexapod positioner as shown in Fig. 14. While examining the beam footprint on a card, the hexapod was moved such that the visible beam was circular and centered in the hole in the primary mirror. Once centered, the RFLEX was used as a focal plane and optical axis reference and thus would not be moved except during movements for FFD measurement, after which it would return to its original position with a repeatability of ±0.5 μm [17].

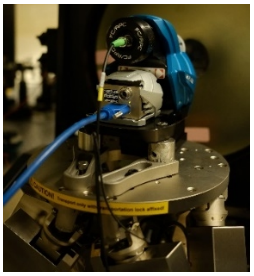

Fig. 14. HASO LIFT 680 Shack Hartmann sensor assembly integrated with PI H-824 hexapod positioner at the back focal plane of the telescope.

When the telescope is highly misaligned, conventional alignment techniques of minimizing astigmatism and coma are useful since the severe misalignment aberrations will dominate over any aberrations caused by form error. Secondary mirror tilts and decenters as well as primary mirror tilts were adjusted to minimize astigmatism and coma while using the reference flat to compensate for resulting tilt aberrations. When coma and astigmatism were minimized as much as possible (all Zernike coefficients $< 0.1\lambda$ @ 635 nm), it became necessary to measure the field dependence of aberrations to continue alignment. The position of the primary mirror was frozen as a new reference and only the secondary mirror was adjusted thereafter. The secondary mirror hexapod and its coordinate system are shown in Fig. 15.

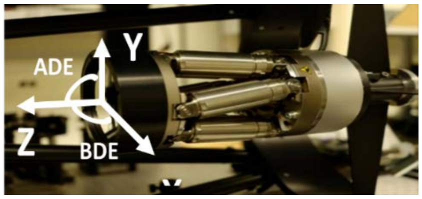

Fig. 15. Secondary mirror mounted on PI H-810 Hexapod positioner shown with local surface coordinate system. ADE and BDE are tilt parameters in the terminology used by CODE V.

From the CODE V model of the telescope with figure error on the primary mirror, the approximate position of the astigmatic nodes was known to be approximately ±0.2 deg. in the X direction. Additionally, the point of symmetry defined by the $\boldsymbol{a}_{222}$ vector is only affected by the alignment, and not figure error [13]. Since the Hilbert telescope has known figure error, placing the POS on the optical axis will indicate the correct alignment. After each movement, the aberration field of astigmatism was measured and examined to determine the position of the nodes and the POS. Coarse measurement grids (5×5 over $\pm 0.2^{\circ}$) were taken at first for rough alignment, and the spacing was decreased as the POS moved closer to the optical axis.

After some iteration in alignment, the astigmatism FFD showed a clearly binodal structure but with only one node clearly visible within the measured field of view. Figure 16 shows the measured FFD for the still misaligned telescope.

The misaligned FFD clearly resembles the magnetic field-like structure described in Section 2.1. In the lower-left quadrant, we see a decrease in the magnitude of the astigmatism followed by a change in the direction of the local astigmatism orientation. Moving in the + X direction, we see

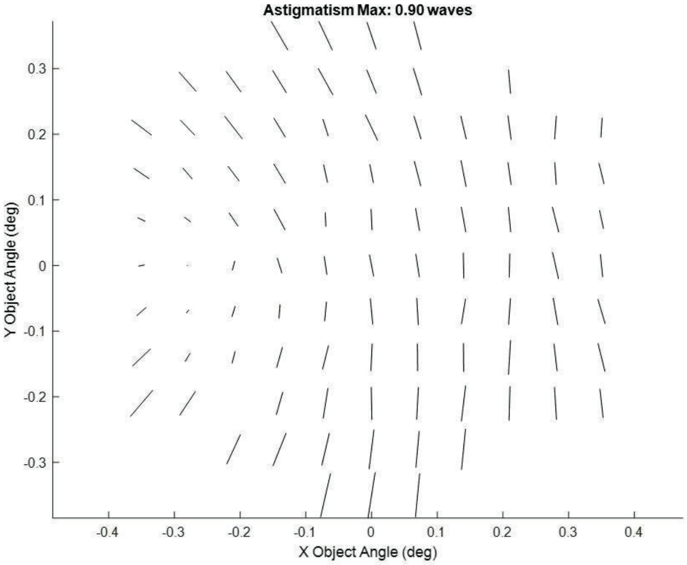

Fig. 16. Measured Zernike astigmatism FFD of misaligned state, exhibiting binodal structure with asymmetric node locations due to misalignment.

the 'field lines' straighten out to indicate proximity to the point of symmetry. This indicates that there should be an additional node in the upper right quadrant that is currently out of view due to alignment. Since a perfectly aligned RC telescope with astigmatic figure error will have both nodes symmetric about the on-axis field, we expect that the secondary mirror has a misalignment in the X/horizontal direction. A horizontal tilt of -0.15 deg. was applied to the H-810 Hexapod and the astigmatism FFD was remeasured.

In the remeasured FFD In Fig. 17, the previously visible node has shifted to the left, and an additional node is now present at the upper-right edge of the measurable field of view. Though collecting points at larger field angles in the upper-right quadrant was prevented by the range of the H-824 Hexapod, the curvature of the lines and change of direction indicated on the figure is evidence of a node in this vicinity. The point of symmetry, indicated by the straight field lines, has also moved much closer to the on-axis field point. We compare the measured misaligned and aligned FFDs above to CODE V simulations in Fig. 18.

There is qualitative agreement between the field-like structure of the measured and simulated FFDs for both the aligned and misaligned cases. Additionally, the node locations in the aligned stated are close to ±0.2 ° in X. There is some discrepancy in the vertical location of the nodes, which is likely a result of a primary mirror clocking error between the CODE V simulation and the real telescope. By only considering the inside of the red boxes of Fig. 18, we observe that the application of the secondary tilt moved the right-most node within the measurable field of view. As expected, Fig. 17 contains evidence of a node in the upper-right quadrant.

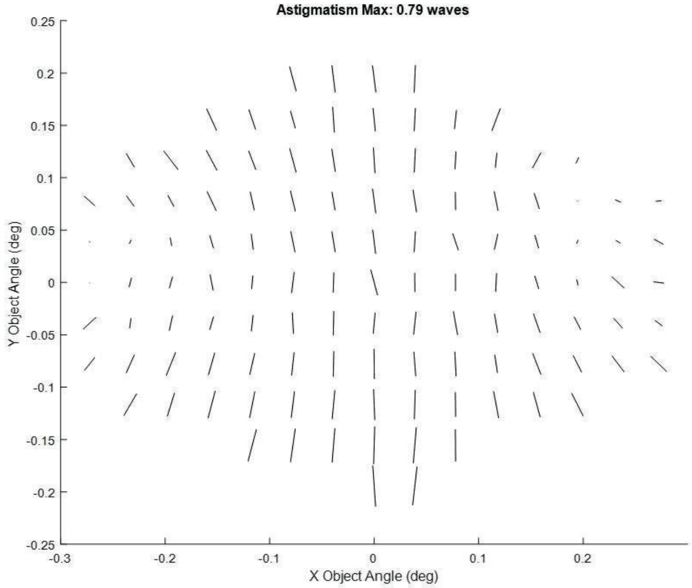

Fig. 17. Measured Astigmatism FFD for the aligned case after applying a -0.15 deg. tilt to the secondary mirror. Red color indicates data points with magnitudes smaller than the errors from fitting indicated above.

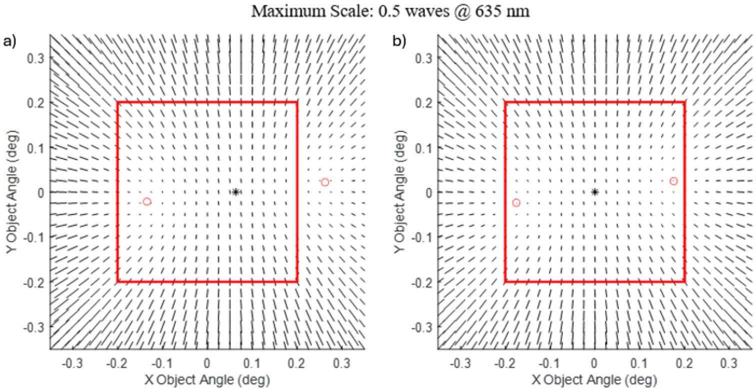

Fig. 18. Simulated Astigmatism FFDs from CODE V showing the -0.15 deg. misaligned state in a) and the nominally aligned state in b). Red boxes represent the approximate field of view covered in measurement, red circles are the node locations, and the black asterisks mark the points of symmetry between the two nodes.

5. Conclusion and future work

In this work, we have laid out and demonstrated a framework to gain insight into the state of alignment of optical systems by using aberration information measured over a large and densely sampled range of the field of view and demonstrated its efficacy in a telescope alignment procedure. Previously, the measurement of densely sampled FFDs has been too impractical for use in the alignment of most optical systems. Zhao *et al.* and Karci *et al.* were the first to our knowledge to demonstrate NAT-predicted behavior using interferometric measurements [10,11,12]. The use of automation and the compact Shack-Hartmann wavefront sensor in this work has allowed us to sample the field of view enough to reveal more of the structure in the FFD than in previous measurements. This approach allows us to predict the presence of nodes outside the field of view and to do so rapidly enough to be useful during optical alignment. Furthermore, the finely sampled set of measurements enables the detection of even slight misalignments to the system.

There are situations in which the minimization of aberrations on-axis is not sufficient for alignment. Schmid describes this risk for two-mirror telescope systems in [18], where a system can appear to be aligned due to having zero astigmatism on-axis but another node is present off axis and astigmatism is not minimized as a whole. As demonstrated in our alignment process, measuring the structure of the FFD can indicate whether this is the case even if the second node is outside of the measured field of view.

Additionally, freeform optical systems often have complicated, non-axisymmetric aberration field patterns which, if measured, can be paired with simulation to indicate the state of alignment. Thus, there is also a need here for more practical methods to measure aberrations through many points in the field of view, and for the accompanying interpretation framework that we have discussed in this paper.

Future work will involve further automating these methods to measure FFDs more rapidly and over a larger field of view. In parallel, we will continue to develop the intuition used in this alignment effort for other aberration types and leveraging higher order aberrations when needed [13].

Funding. Hilbert Family (Angela, Daniel, and David Hilbert); Synopsys; R.E. Hopkins Center at the University of Rochester; National Science Foundation Industry-University Cooperative Research Centers REU Program of the Center for Freeform Optics (IIP-1338877, IIP-1338898, IIP-1822026, IIP-1822049); Fulbright Association (FY-2019-TR-PD-06).

Acknowledgments. We thank Imagine Optic, Inc. for their contribution of the HASO LIFT 680 + RFLEX wavefront sensor system and their support for integration. We also thank Professor James Fienup for the loan of the H-824 Hexapod. Finally, we would like to acknowledge Jonathan Papa, Aaron Bauer, and Yuchen Wu for stimulating discussions about this project and Jules Esen for her contribution to measuring the reference mirror dynamic tilt. We thank Synopsys Inc. for providing an academic license of CODE V.

Disclosures. The authors declare there are no conflicts of interest related to this article.

Data availability. Data underlying the results presented in this paper are not publicly available at this time but may be obtained from the authors upon reasonable request.

References

1. R. V. Shack and K. Thompson, "Influence of alignment errors of a telescope system on its aberration field," in *Optical Alignment I* (SPIE, 1980), 0251, pp. 146–153.
2. K. Thompson, "Description of the third-order optical aberrations of near-circular pupil optical systems without symmetry," J. Opt. Soc. Am. A **22**(7), 1389–1401 (2005).
3. K. Fuerschbach, J. P. Rolland, and K. P. Thompson, "Nodal aberration theory applied to freeform surfaces," in *Classical Optics 2014 (2014), Paper ITh2A.5* (Optica Publishing Group, 2014), p. ITh2A.5.
4. K. Fuerschbach, J. P. Rolland, and K. P. Thompson, "Theory of aberration fields for general optical systems with freeform surfaces," Opt. Express **22**(22), 26585–26606 (2014).
5. A. Bauer, E. M. Schiesser, and J. P. Rolland, "Starting geometry creation and design method for freeform optics," Nat. Commun. **9**(1), 1756 (2018).
6. A. Bauer and J. P. Rolland, "Roadmap for the unobscured three-mirror freeform design space," Opt. Express **29**(17), 26736–26744 (2021).

7. J. P. Rolland, A. M. Bauer, K. H. Fuerschbach, *et al.*, eds. (SPIE, 2020), p. 14.
8. T. Schmid, J. P. Rolland, A. Rakich, *et al.*, "Separation of the effects of astigmatic figure error from misalignments using Nodal Aberration Theory (NAT)," Opt. Express **18**(16), 17433–17447 (2010).
9. T. Schmid, "Misalignment induced nodal aberration fields and their use in the alignment of astronomical telescopes," Electron. Theses Diss. (2010).
10. N. Zhao, J. C. Papa, K. Fuerschbach, *et al.*, "Experimental investigation in nodal aberration theory (NAT) with a customized Ritchey-Chrétien system: third-order coma," Opt. Express **26**(7), 8729–8743 (2018).
11. Ö. Karcı, E. Arpa, M. Ekinci, *et al.*, "Experimental investigation of binodal astigmatism in nodal aberration theory (NAT) with a Cassegrain telescope system," Opt. Express **29**(13), 19427–19440 (2021).
12. Ö. Karcı, M. Yeşiltepe, E. Arpa, *et al.*, "Experimental investigation in nodal aberration theory (NAT): separation of astigmatic figure error from misalignments in a Cassegrain telescope," Opt. Express **30**(7), 11150–11164 (2022).
13. J. Sebag, W. Gressler, T. Schmid, *et al.*, "LSST telescope alignment plan based on nodal aberration theory," Publ. Astron. Soc. Pac. **124**(914), 380–390 (2012).
14. Physik Instrumente (PI) GmbH & Co. KG, "H-810 hexapod microrobot user manual," (2013).
15. . "HASO LIFT 680 Wavefront Sensor," https://www.imagine-optic.com/products/haso-lift-680-wavefront-sensor/.
16. . Physik Instrumente (PI) GmbH & Co. KG, "H-824 hexapod microrobot user manual," (2023).
17. R. Gray and J. Howard, "ZernikeCalc," (2013).
18. T. Schmid, K. P. Thompson, and J. P. Rolland, "A unique astigmatic nodal property in misaligned Ritchey-Chrétien telescopes with misalignment coma removed," Opt. Express **18**(5), 5282–5288 (2010).